

Spin depolarization induced by self-generated magnetic fields during cylindrical implosionsRonghao Hu , Hao Zhou, Zhihao Tao, and Meng Lv**College of Physics, Sichuan University, Chengdu, 610065, China;**Key Laboratory of High Energy Density Physics and Technology,**Ministry of Education, Sichuan University, Chengdu, 610064, China;**and Key Laboratory of Radiation Physics and Technology, Ministry of Education, Sichuan University, Chengdu, 610064, China*

Shiyang Zou and Yongkun Ding

Institute of Applied Physics and Computational Mathematics, Beijing, 100094, People's Republic of China (Received 26 June 2020; revised 28 September 2020; accepted 10 October 2020; published 26 October 2020)

Spin-polarized fuels are promising for inertial confinement fusion due to the enhanced fusion cross section. One significant concern of spin-polarized inertial confinement fusion is whether the nuclei polarization could survive in the implosions and contribute to ignitions. Here we present numerical simulation methods and results of spin dynamics of polarized deuterium-tritium fuels in strong self-generated magnetic fields during the implosions of dense cylindrical shells. The magnetic field generation and evolution is modeled with generalized Ohm's laws combined with hydrodynamic equations. The spin dynamics is investigated with a particle-tracking method, by solving the spin precession equations of tracked particles. Rayleigh-Taylor instabilities and Richtmyer-Meshkov instabilities are found to be the main cause of depolarization. Hydrodynamic instabilities lead to depolarization of nuclei near the hot-spot shell interface, and an asymmetric shock front leads to depolarization of nuclei inside a hot spot. Deuterium polarization is more stable than tritium polarization due to its smaller gyromagnetic ratio. Low-mode perturbations can lead to higher depolarization inside a hot spot than high-mode perturbations. In the multimode simulations, the modes around 16–32 are significant for hot-spot depolarization.

DOI: [10.1103/PhysRevE.102.043215](https://doi.org/10.1103/PhysRevE.102.043215)**I. INTRODUCTION**

For controlled thermonuclear fusion, using spin polarized deuterium-tritium (DT) fuels can be advantageous in providing control of the reaction rates and the angular distribution of the reaction products [1–3]. Fusion reaction rates are critical to the fusion energy generation. It was estimated [1] that the cross section can be enhanced by a factor of $\delta = 1.5$ when the spins of DT are perfectly aligned in a total spin 3/2 configuration and assuming that the reaction is isotropic. Recently, *ab initio* predictions [4] including anisotropies show that the enhancement factor δ can be larger than 1.5 at certain energies. For inertial confinement fusion (ICF), one-dimensional simulations of directly driven capsules show that the required laser power and energy to achieve a high gain scale as $\delta^{-0.6}$ and $\delta^{-0.4}$, respectively, while the maximum achievable energy gain scales as $\delta^{0.9}$ [5]. The required hot-spot temperature and areal density for ignition can both be reduced by about 15% for a fully polarized nuclear fuel [5]. Two-dimensional (2D) simulations indicate that the effects due to anisotropic reaction product emission and deposition can be neglected in spin-polarized high-gain ICF targets [6]. Several techniques have been developed to produce polarized DT fuels such as the atomic beam source [7], static nuclear polarization [8], dynamic nuclear polarization [9],

spin-exchange optical pumping [10,11], and ultraviolet photodissociation [12]. The polarization of deuterium or tritium atoms can reach a high level of about 90% [3,7].

Depolarization is a significant concern in polarized fusion [1,2]. The two main depolarization mechanisms are collisional depolarization and magnetic-field-induced depolarization. Simple estimations by More [2] show that depolarization can be negligible during the short duration of ICF implosions. One-dimensional simulations show that collisional depolarization can be smaller than 0.1% during the compression and burn phase [13]. Recently, simulations [14,15] and experiments [16–18] have shown self-generated magnetic fields in ICF plasmas in excess of 10^3 T, which is much larger than the estimations of More [2]. These magnetic fields are generated by the baroclinic source terms during the onset of hydrodynamic instabilities. Rayleigh-Taylor instability (RTI) and Richtmyer-Meshkov instability (RMI) arise from low-mode and high-mode asymmetries typically seeded by the nonuniformity of the drivers and DT ice roughness of the inner shell surface, which are currently unavoidable for both indirect drive and direct drive implosions [19,20]. RTI occurs in the deceleration phase of the implosion when the pressure gradient is in the opposite direction from the density gradient [21,22]. RMI occurs when a shock wave passes through the interface between the two fluids with different densities [23]. While RTI and RMI generate strong magnetic fields near the interface, the shock front distortion [24] related to RMI can also generate magnetic

*Corresponding author: lvmengphys@scu.edu.cn

fields as the shock propagates inside the hot spot. Depolarization inside the hot spot is critical to the ignition and fusion energy output. The DT nuclei inside the hot spot need to stay polarized over the ICF confinement time in an order of 10^{-10} s [25]. For magnetic fields of 10^3 T [26], the periods of Larmor precession for DT nuclei are 1.53×10^{-10} s and 2.20×10^{-11} s, respectively, which are comparable to or even shorter than the ICF confinement time. The depolarization induced by self-generated magnetic fields thus cannot be neglected for spin-polarized ICF.

In this paper, we present simulation methods and results of DT depolarization in self-generated magnetic fields during the implosions of cylindrical shells. The magnetic field generation and evolution is modeled with generalized Ohm's laws combined with hydrodynamic equations. The spin dynamics is investigated with a particle-tracking method, by solving the spin precession equations of tracked particles. In the single-mode simulations, RTI and RMI generate strong magnetic fields in excess of 10^3 T, leading to depolarization of nuclei near the hot-spot shell interface. Shock front distortion related to RMI generates magnetic fields on the order of 10^2 T inside the hot spot. Deuterium polarization is more stable than tritium polarization due to its smaller gyromagnetic ratio. The cross-sectional enhancement factor δ drops to below 1.1 near the interface, while δ drops to about 1.2 inside the hot spot. Low-mode perturbations can lead to higher depolarization inside a hot spot than high-mode perturbations. In the multi-mode simulations, the resulted fusion cross sections inside hot spot are about 30% higher than the unpolarized cross sections.

II. SIMULATION METHODS

In our spin dynamics simulation code SpinSim, we solve hydrodynamics equations and a magnetic field evolution equation with the finite volume method and the spin precession equation with the particle-tracking method. The hydrodynamics equations and spin precession equation can be derived from a rigorous kinetic description of spin-polarized plasmas [27,28]. The kinetics equations are difficult to solve numerically for higher dimensions due to the extra dimensions in phase space. The particle-tracking method can be easily coupled with hydrodynamics simulations and particle-in-cell simulations, which are the predominant numerical tools to investigate ICF.

The equations of compressible inviscid hydrodynamics can be written in the form of conservation laws,

$$\frac{\partial U}{\partial t} + \frac{\partial F_x}{\partial x} + \frac{\partial F_y}{\partial y} + \frac{\partial F_z}{\partial z} = S. \quad (1)$$

The conserved variable U is

$$U = (\rho, \rho v_x, \rho v_y, \rho v_z, \rho E)^T, \quad (2)$$

where ρ is mass density, $v_{\{x,y,z\}}$ are the three components of velocity, $E = \rho v^2/2 + E_{\text{int}}$ is the total energy, and E_{int} is the internal energy. The fluxes are

$$F_x = (\rho v_x, \rho v_x^2 + p, \rho v_x v_y, \rho v_x v_z, [E + p]v_x)^T, \quad (3)$$

$$F_y = (\rho v_y, \rho v_x v_y, \rho v_y^2 + p, \rho v_y v_z, [E + p]v_y)^T, \quad (4)$$

$$F_z = (\rho v_z, \rho v_x v_z, \rho v_y v_z, \rho v_z^2 + p, [E + p]v_z)^T. \quad (5)$$

The sources S here are zeros. The ideal gas equation of state is used with an adiabatic index of $5/3$. The evolution equation of the magnetic field including the Biermann battery source can be written as [29]

$$\begin{aligned} \frac{\partial \mathbf{B}}{\partial t} &= \nabla \times (\mathbf{v} \times \mathbf{B}) + \nabla \times \frac{\nabla p_e}{n_e e} \\ &= \nabla \times (\mathbf{v} \times \mathbf{B}) + \frac{m_i}{e} \frac{1}{1 + \chi} \frac{\nabla p \times \nabla \rho}{\rho^2}. \end{aligned} \quad (6)$$

Here p_e is the electron pressure, n_e is the electron number density, e is the elementary charge, m_i is the average ion mass, and χ is the ionization fraction. For equimolar DT fuel, $m_i \approx 2.5m_p$, where m_p is the proton mass, and $\chi \approx 1$. Equation (6) can be written in the form of Eq. (1), with

$$U = (B_x, B_y, B_z)^T, \quad (7)$$

$$F_x = (0, v_x B_y - v_y B_x, v_x B_z - v_z B_x)^T, \quad (8)$$

$$F_y = (v_y B_x - v_x B_y, 0, v_y B_z - v_z B_y)^T, \quad (9)$$

$$F_z = (v_z B_x - v_x B_z, v_z B_y - v_y B_z, 0)^T, \quad (10)$$

$$S = \frac{m_i}{e} \frac{1}{1 + \chi} \frac{\nabla p \times \nabla \rho}{\rho^2}. \quad (11)$$

The magnetic force on the fluid flow is neglected as the ratio of thermal pressure to magnetic pressure $\beta = \frac{p}{B^2/(2\mu_0)} \gg 1$ for a magnetic field on the order of 10^3 T and pressure over 10^{14} Pa in ICF plasmas. The conservation laws (1) are solved using the finite volume method on Cartesian grids [30]. The Harten-Lax-van Leer approximate Riemann solver is used to calculate the fluxes on computation cell interfaces. A second-order Runge-Kutta scheme is used for temporal integration [30]. The Biermann sources (11) are calculated using the central difference scheme.

We use macroparticles to model DT nuclei with similar initial locations. The weight of a macroparticle is the number of nuclei included,

$$w_i = \frac{\rho_{\text{cell}} V_{\text{cell}}}{N_{\text{cell}} m_i}, \quad (12)$$

where ρ_{cell} and V_{cell} are the density and volume of the initial cell, respectively, and N_{cell} is the total number of macroparticles in that cell. N_{cell} is fixed in the simulation domain, and the initial positions of the particles are randomized within the cell. The positions of the particles are changed according to

$$\frac{d\mathbf{x}_i}{dt} = \mathbf{v}_{\text{cell}}, \quad (13)$$

where \mathbf{v}_{cell} is the fluid velocity of the located cell. The spin evolution of particles is modeled using the spin precession equation [2,31,32]

$$\frac{d\mathbf{s}_i}{dt} = \gamma \mathbf{s}_i \times \mathbf{B}_{\text{cell}}, \quad (14)$$

where \mathbf{B}_{cell} is the magnetic field of the located cell, and the gyromagnetic ratio $\gamma = 4.1065 \times 10^7$ and 2.8535×10^8 $\text{rad s}^{-1} \text{T}^{-1}$ for DT nuclei, respectively [33]. Equation (14) is solved using a semianalytic method by rotating the spin vector \mathbf{s}_i in the constant magnetic field \mathbf{B}_{cell} within

a computation time step and $s_i^2 = 1$ is preserved numerically. The collisional depolarization is neglected in our simulation.

The cross-sectional enhancement factor δ of $D(T, n)^4He$ reaction with arbitrary spin configuration can be estimated as [1,31,32]

$$\delta \approx \frac{3}{2}a + b + \frac{1}{2}c, \quad (15)$$

where $a = d_1 t_{1/2} + d_{-1} t_{-1/2}$, $b = d_0(t_{1/2} + t_{-1/2}) = d_0$, $c = d_1 t_{-1/2} + d_{-1} t_{1/2}$, $d_{\{1,0,-1\}}$ is the fractions of deuterium nuclei at $m = \{1, 0, -1\}$ states, $t_{\{1/2, -1/2\}}$ is the fractions of tritium nuclei at $m = \{1/2, -1/2\}$ state, and m is the spin quantum number. With the spin of DT nuclei initially polarized along the $+x$ direction, the fractions of deuterium nuclei can be calculated using the spin vectors of macroparticles [1,31,32]

$$d_1 = \frac{\sum_i w_i (1 + s_{xi})^2 / 4}{\sum_i w_i}, \quad d_0 = \frac{\sum_i w_i (1 - s_{xi}^2) / 2}{\sum_i w_i},$$

$$d_{-1} = \frac{\sum_i w_i (1 - s_{xi})^2 / 4}{\sum_i w_i}. \quad (16)$$

For tritium nuclei,

$$t_{1/2} = \frac{\sum_i w_i (1 + s_{xi}) / 2}{\sum_i w_i}, \quad t_{-1/2} = \frac{\sum_i w_i (1 - s_{xi}) / 2}{\sum_i w_i}. \quad (17)$$

The particle-tracking algorithm can be easily parallelized without data races as there are no interactions between macroparticles. We have implemented these algorithms in the simulation code SpinSim running on a graphics processing unit.

III. IMPLOSION SIMULATIONS

To investigate spin depolarization in strong magnetic fields generated by hydrodynamic instabilities during implosions, 2D simulations of cylindrical implosions are performed using a high-density shell imploding a low-density hot spot [34,35]. Cylindrical implosions can be well diagnosed in experiments, providing an excellent platform to validate modeling for convergent geometries [36]. The low-density hot spot is located inside a radial distance of $r_1 = 295 \mu\text{m}$, with homogeneous density $\rho_1 = 0.5 \text{ g/cm}^3$ and pressure $p_1 = 5 \times 10^{14} \text{ Pa}$. The density linearly rises to $\rho_2 = 10 \text{ g/cm}^3$ from r_1 to $r_2 = 305 \mu\text{m}$. The shell is located from r_2 to $r_3 = 345 \mu\text{m}$ with a constant density ρ_2 . The pressure increases linearly from p_1 to $p_2 = 1 \times 10^{16} \text{ Pa}$ with radial distance from r_1 to r_3 . The density linearly drops to $\rho_3 = 0.1 \text{ g/cm}^3$, and the pressure drops to $p_3 = 1 \times 10^{12} \text{ Pa}$ with the radius increased to $r_4 = 355 \mu\text{m}$. The density and pressure remain constant for the region outside r_4 . The initial fluid velocities and magnetic fields are all zeros. The simulations are performed on 2000×2000 grid cells without refinement. The simulation domain has a size of $-500 \mu\text{m} \leq x, y \leq 500 \mu\text{m}$. Outflow boundaries are used in all directions. Here 4×10^6 macroparticles for DT nuclei are initially located uniformly in the simulation domain.

The evolution of density and pressure without perturbation is shown in Fig. 1. The surface of the shell is initially very hot, and matter in the surface starts moving outwards, compressing the hot spot with rocket effect. A shock wave is launched and

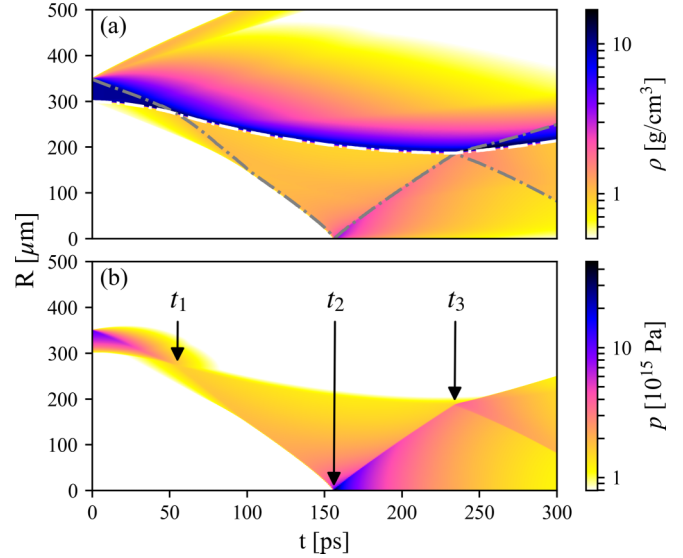


FIG. 1. (a) Time evolution of the mass density ρ radial profile in the implosion without initial perturbation. The interface of the hot spot and shell is marked by a white dashed-dotted line, and the shock front position is marked by gray dashed-dotted lines. (b) Time evolution of pressure p .

converges towards the center, increasing the density and pressure of the hot spot, rebounds on itself, and propagates again outwards, as shown in Figs. 1(a) and 1(b). The convergence ratio is about 1.5 in our simulations. At about $t_1 = 56 \text{ ps}$, the shock propagates through the hot-spot shell interface, causing the RMI growth. After t_1 , the gradients of density and pressure near the interface become antiparallel, and the interface becomes unstable to RTI [22]. At $t_2 = 157 \text{ ps}$, the shock rebounds on itself in the center and then reaches the interface again at $t_3 = 235 \text{ ps}$.

Single-mode perturbations are imposed on the interface of hot spot and shell, $\delta r = A \cos(m\theta)$, where A is the initial amplitude of perturbation, m is the mode number, and θ is the polar angle. The perturbation is added to r_1 and r_2 . The simulation results for $m = 16$, $A = 10 \mu\text{m}$ are shown in Fig. 2. The perturbations grow into spikes and bubbles due to RMI and RTI near the interface as shown in Fig. 2(a). The “mushroom caps” are developed around the tips of spikes due to the Kelvin-Helmholtz instability [14]. Petaloid structure can be observed in the pressure distribution as depicted in Fig. 2(b). This is because the convergence of the shock is affected by the initial perturbation. When the shock wave passes through the corrugated interface, the RMI are triggered and the shock wave itself is also distorted by the RMI [24]. As the shock propagates, the perturbation field is left behind in the shocked fluid. The shock interference leads to the petaloid structure and nonuniform heating of the hot spot. The most intense magnetic fields are found surrounding the spikes and bubbles near the interface as displayed in Fig. 2(c). The density gradient is large near the interface, and when perturbations are present, the density gradient is misaligned with the pressure gradient. The distorted shock front also generates magnetic fields inside the hot spot as shown in Fig. 2(c). The fractions of depolarized deuterium ($d_0 + d_{-1}$) and tritium ($t_{-1/2}$) are

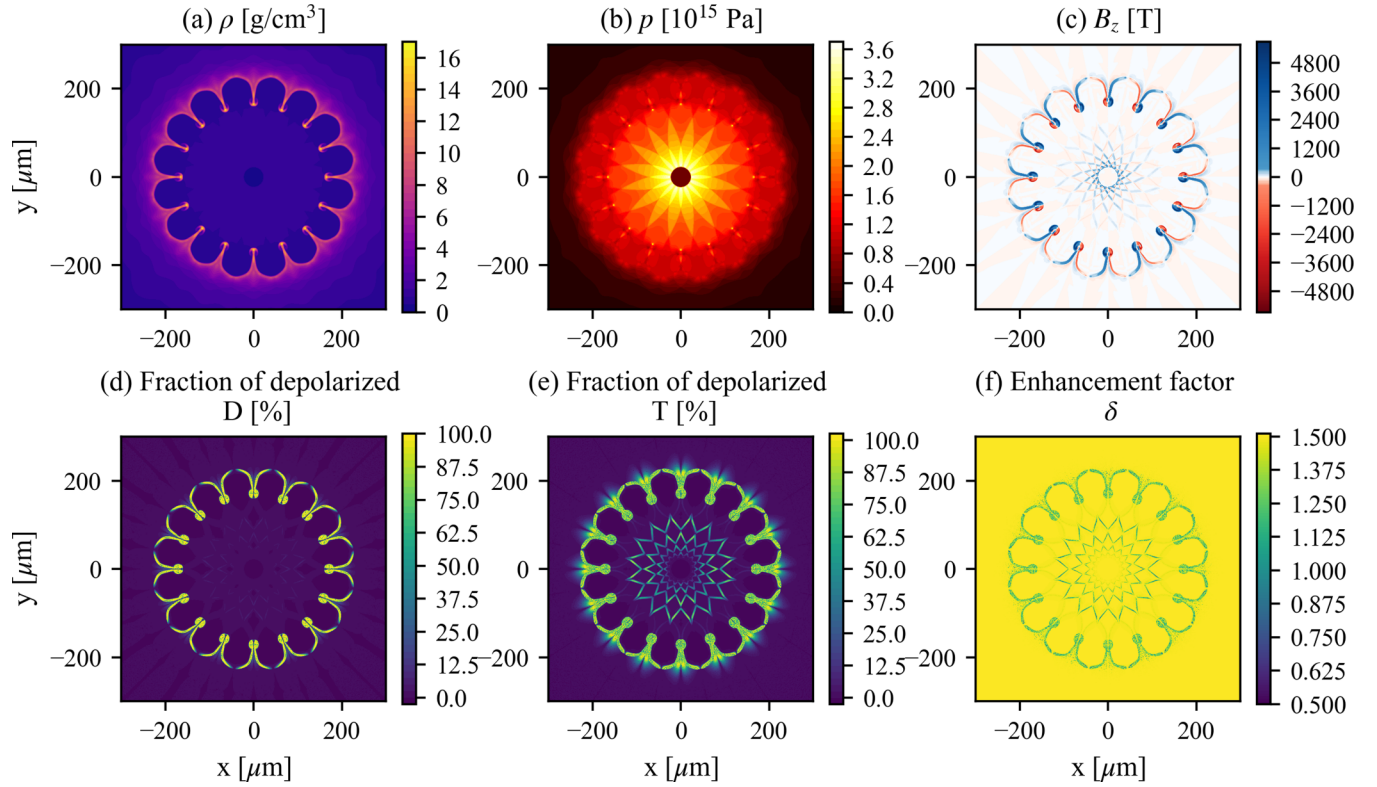


FIG. 2. Simulation results for initial perturbation $m = 16$ and $A = 10 \mu\text{m}$ at $t = 150$ ps: (a) the distribution of mass density ρ , (b) pressure p , (c) magnetic fields B_z , (d) fraction of depolarized D, (e) fraction of depolarized T, (f) cross-sectional enhancement factor δ .

shown in Fig. 2(d) and Fig. 2(e), respectively. The depolarized deuterium and tritons are mostly located around the spikes where the magnetic fields are strong. More depolarized tritons are found inside the hot spot than deuterium. The cross-sectional enhancement factor calculated by Eq. (15) is shown in Fig. 2(f). The enhancement factor δ is smaller than 1.5 near the hot-spot shell interface and some regions inside the hot spot. The structures of magnetic fields and the enhancement factor inside the hot spot resemble the interference pattern of the distorted shock, showing that the breaking of shock convergence leads to magnetic field growth and depolarization inside the hot spot.

For the central hot-spot ignition scheme, the ignition process starts from the central low-density hot fuel [19]. Depolarization in the central region is extremely harmful to the ignition of the polarized fusion target. To diagnose the depolarization inside the hot spot, we divide the hot spot and shell into two regions, the inner region from $r = 0$ to $75 \mu\text{m}$ and the outer region from $r = 75$ to $350 \mu\text{m}$. The inner region is mostly affected by the asymmetry shock wave, and the outer region is affected by the RMI and RTI. The simulation results of averaged magnetic field strength, fractions of depolarized DT, and enhancement factor in the inner and outer regions are shown in Fig. 3. The initial perturbation mode is fixed at $m = 16$, and the initial perturbation amplitude is varied from $A = 1.0$ to $25 \mu\text{m}$. The magnetic field in the inner region starts to grow after the shock enters and reaches a maximum when the shock converges at the center as shown in Fig. 3(a). After the shock rebounds, the gradient of density flips into its opposite direction, and the magnetic field decreases as

the Biermann term also changes its direction. The maximum magnetic field strength around 150 ps increases with the initial perturbation amplitude, but the increment seems to saturate after $A = 10 \mu\text{m}$. When the initial perturbation amplitude is large, the spikes of RTI can penetrate into the inner region and cause the magnetic field to grow as the curve of $A = 25 \mu\text{m}$ after 250 ps in Fig. 3(a). The fractions of depolarized deuterons in the inner region are smaller than 1% except for the $A = 25 \mu\text{m}$ case as shown in Fig. 3(b). The fractions of depolarized tritons in the inner region are more than 10 times larger than the deuterons as shown in Fig. 3(c). The enhancement factor δ starts to decrease as the magnetic field grows as shown in Fig. 3(d). δ is larger than 1.2 even for the worst case of $A = 25 \mu\text{m}$. The magnetic field in the outer region starts to grow earlier due to the RMI and RTI growth as shown in Fig. 3(e). The magnetic field strength in the outer region is also much larger than the inner region. The magnetic field strength in the outer region increases as the initial perturbation amplitude increases. The fractions of depolarized deuterons in the outer region are more than 10 times larger than those in the inner region as shown in Fig. 3(f). The fractions of depolarized tritons in the outer region are only a few times larger than those in the inner region as shown in Fig. 3(g). The cross-sectional enhancement factors δ in the outer region are much lower than those in the inner region as shown in Fig. 3(h). δ in the outer region also decreases monotonically as the initial perturbation increases from 1 to $25 \mu\text{m}$. Controlling the initial perturbation amplitude is necessary for reducing the depolarization in both the inner and outer regions.

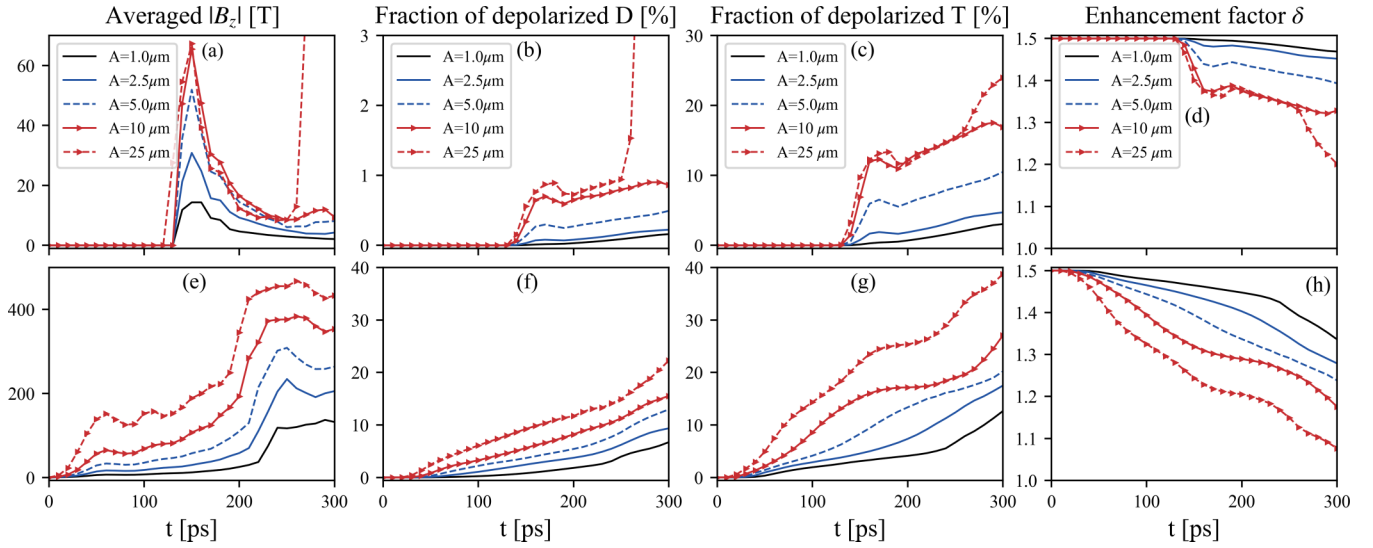


FIG. 3. Simulation results for different initial perturbation amplitudes A with fixed $M = 16$. (a) Mass weighted average magnetic field strength $|B_z|$ in the inner region. (b) Fraction of depolarized deuterons in the inner region. (c) Fraction of depolarized tritons in the inner region. (d) Cross-sectional enhancement factor δ in the inner region. (e) Mass weighted average magnetic field strength $|B_z|$ in the outer region. (f) Fraction of depolarized deuterons in the outer region. (g) Fraction of depolarized tritons in the outer region. (h) Cross-sectional enhancement factor δ in the outer region.

The simulation results for different mode numbers of the initial perturbations are shown in Fig. 4. The peak averaged magnetic field strength in the inner region first increases with mode number, reaches a maximum for $m = 16$, and then decreases as the mode number increases further as shown in Fig. 4(a). The averaged magnetic field strength for $m = 8$ after the peak is larger than that for $m = 16$, and the cross-sectional enhancement factor is the lowest for $m = 8$ and largest for

$m = 64$ as shown in Fig. 4(b). The averaged magnetic field in the outer region for $m \geq 16$ can reach over 200 T as shown in Fig. 4(c), and δ in the outer region decreases as the mode number increases as shown in Fig. 4(d). The polarization in the inner region is more stable to high-mode perturbations, while the polarization in the outer region is more stable to low-mode perturbations.

Simulations of random multiple modes are performed, and the results are shown in Fig. 5. The initial perturbations can

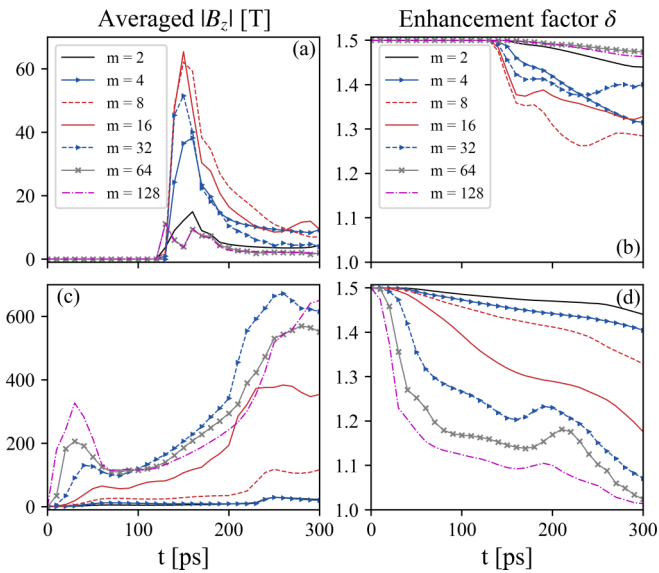


FIG. 4. Simulation results for different initial perturbation mode numbers m with fixed $A = 10 \mu\text{m}$. (a) Mass weighted average magnetic field strength $|B_z|$ in the inner region. (b) Cross-sectional enhancement factor δ in the inner region. (c) Mass weighted average magnetic field strength $|B_z|$ in the outer region. (d) Cross-sectional enhancement factor δ in the outer region.

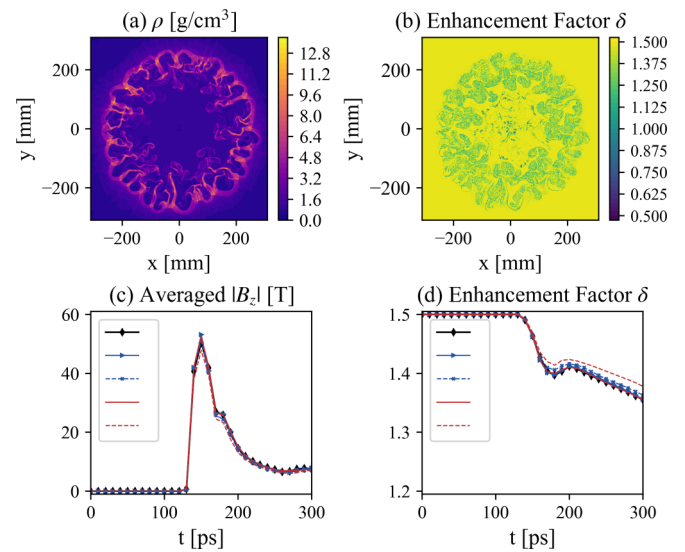


FIG. 5. Multimode random perturbation simulation results. (a) Density ρ at 150 ps. (b) Cross-sectional enhancement factor δ at 150 ps. (c) Mass weighted average magnetic field strength $|B_z|$ in the inner region for five random initial perturbations. (d) Cross-sectional enhancement factor δ in the inner region for five random initial perturbations.

be written as $\delta r = \sum_m A_m \cos(m\theta + \phi_m)$, with m from 1 to 128. The amplitudes A_m are randomly chosen from 0 to $1 - 0.0025(m - 1) \mu\text{m}$ and phases ϕ_m are randomly chosen from 0 to 2π . The density distribution is shown in Fig. 5(a). The spikes of RTI and RMI are more curvy than the single mode results, and they can interact with each other. The interaction between modes cause the modes around 16–32 to grow significantly as shown in Fig. 5(a). The cross-sectional enhancement factor δ is small around the spikes, and there are also some depolarized fuels near the center as shown in Fig. 5(b). The simulation results are similar for five random initial perturbations as shown in Figs. 5(c) and 5(d). The evolutions of averaged magnetic field strength and cross-sectional enhancement factor δ are similar to the results of $m = 16$ and $m = 32$ in Fig. 4. The enhancement factor δ is still larger than 1.3 as shown in Fig. 5(d).

IV. DISCUSSION

In summary, we have combined the hydrodynamics simulation with a particle-tracking method to investigate the spin dynamics of polarized deuterons and tritons during cylindrical implosions. In the single-mode simulations, RTI and RMI

generate strong magnetic fields in excess of 10^3 T, leading to depolarization of nuclei near the hot-spot shell interface. Shock front distortion related to RMI generates magnetic fields on the order of 10^2 T inside the hot spot. The inner zone of the hot spot has smaller self-generated magnetic fields and a larger cross-sectional enhancement factor than the outer zone where RMI and RTI happens. The cross-sectional enhancement factor decreases as the initial perturbation amplitudes increase. The polarization in the inner zone of hot spot is more stable to high-mode perturbations while the polarization in the outer zone is more stable to low-mode perturbations. In the multimode random perturbation simulations, the modes around 16–32 are significant for depolarization. Our results indicate that controlling hydrodynamic instabilities and drive asymmetries is significant for preserving the polarization in spin-polarized ICF. The polarization of D nuclei is more stable than the polarization of T nuclei during the implosion. Spin-polarized DD fusion also can be considered to power future fusion reactors. Our preliminary simulations include only magnetic-field-induced depolarization and cylindrical implosion hydrodynamics. Further investigations of spin-polarized fusion including collisional depolarization, spherical implosion, radiation transport, fusion reactions, and alpha particle deposition are planned for the future.

-
- [1] R. M. Kulsrud, H. P. Furth, E. J. Valeo, and M. Goldhaber, Fusion Reactor Plasmas with Polarized Nuclei, *Phys. Rev. Lett.* **49**, 1248 (1982).
 - [2] R. M. More, Nuclear Spin-Polarized Fuel in Inertial Fusion, *Phys. Rev. Lett.* **51**, 396 (1983).
 - [3] G. Ciullo, R. Engels, M. Büscher, and A. Vasilyev, *Nuclear Fusion with Polarized Fuel* (Springer International Publishing, Cham, 2016).
 - [4] G. Hupin, S. Quaglioni, and P. Navrátil, *Ab initio* predictions for polarized deuterium-tritium thermonuclear fusion, *Nat. Commun.* **10**, 351 (2019).
 - [5] M. Temporal, V. Brandon, B. Canaud, J. Didelez, R. Fedosejevs, and R. Ramis, Ignition conditions for inertial confinement fusion targets with a nuclear spin-polarized DT fuel, *Nucl. Fusion* **52**, 103011 (2012).
 - [6] Y. Pan and S. Hatchett, Spin-polarized fuel in high gain ICF targets, *Nucl. Fusion* **27**, 815 (1987).
 - [7] A. Roberts, P. Elmer, M. Ross, T. Wise, and W. Haerberli, Medium field RF transitions for polarized beams of hydrogen and deuterium, *Nucl. Instrum. Methods Phys. Res. A* **322**, 6 (1992).
 - [8] S. Bouchigny and J.-P. Didelez, Towards the polarization of DT molecules, *Nucl. Instrum. Methods Phys. Res. A* **577**, 320 (2007).
 - [9] P. C. Souers, R. T. Tsugawa, E. M. Fearon, G. W. Collins, J. L. Maienschein, R. A. Failor, E. R. Mapoles, and P. A. Fedders, Nuclear polarization of solid deuterium-tritium, *J. Vac. Sci. Technol.* **11**, 2827 (1993).
 - [10] S. G. Redsun, R. J. Knize, G. D. Cates, and W. Happer, Production of highly spin-polarized atomic hydrogen and deuterium by spin-exchange optical pumping, *Phys. Rev. A* **42**, 1293 (1990).
 - [11] B. Clasie, C. Crawford, J. Seely, W. Xu, D. Dutta, and H. Gao, Laser-driven target of high-density nuclear-polarized hydrogen gas, *Phys. Rev. A* **73**, 020703(R) (2006).
 - [12] D. Sofikitis, P. Glodic, G. Koumariou, H. Jiang, L. Bougas, P. C. Samartzis, A. Andreev, and T. P. Rakitzis, Highly Nuclear-Spin-Polarized Deuterium Atoms from the UV Photodissociation of Deuterium Iodide, *Phys. Rev. Lett.* **118**, 233401 (2017).
 - [13] B. Goel and W. Heeringa, Spin polarized ICF targets, *Nucl. Fusion* **28**, 355 (1988).
 - [14] B. Srinivasan, G. Dimonte, and X.-Z. Tang, Magnetic Field Generation in Rayleigh-Taylor Unstable Inertial Confinement Fusion Plasmas, *Phys. Rev. Lett.* **108**, 165002 (2012).
 - [15] C. A. Walsh, J. P. Chittenden, K. McGlinchey, N. P. L. Niasse, and B. D. Appelbe, Self-Generated Magnetic Fields in the Stagnation Phase of Indirect-Drive Implosions on the National Ignition Facility, *Phys. Rev. Lett.* **118**, 155001 (2017).
 - [16] M. J.-E. Manuel, C. K. Li, F. H. Séguin, J. Frenje, D. T. Casey, R. D. Petrasso, S. X. Hu, R. Betti, J. D. Hager, D. D. Meyerhofer, and V. A. Smalyuk, First Measurements of Rayleigh-Taylor-Induced Magnetic Fields in Laser-Produced Plasmas, *Phys. Rev. Lett.* **108**, 255006 (2012).
 - [17] L. Gao, P. M. Nilson, I. V. Igumenshev, S. X. Hu, J. R. Davies, C. Stoeckl, M. G. Haines, D. H. Froula, R. Betti, and D. D. Meyerhofer, Magnetic Field Generation by the Rayleigh-Taylor Instability in Laser-Driven Planar Plastic Targets, *Phys. Rev. Lett.* **109**, 115001 (2012).
 - [18] I. V. Igumenshev, A. B. Zylstra, C. K. Li, P. M. Nilson, V. N. Goncharov, and R. D. Petrasso, Self-generated magnetic

- fields in direct-drive implosion experiments, *Phys. Plasmas* **21**, 062707 (2014).
- [19] R. Betti and O. A. Hurricane, Inertial-confinement fusion with lasers, *Nat. Phys.* **12**, 435 (2016).
- [20] J. R. Peterson, B. M. Johnson, and S. W. Haan, Instability growth seeded by dt density perturbations in ICF capsules, *Phys. Plasmas* **25**, 092705 (2018).
- [21] Z. Fan, S. Zhu, W. Pei, W. Ye, M. Li, X. Xu, J. Wu, Z. Dai, and L. Wang, Numerical investigation on the stabilization of the deceleration phase Rayleigh-Taylor instability due to alpha particle heating in ignition target, *Europhys. Lett.* **99**, 65003 (2012).
- [22] A. Bose, K. M. Woo, R. Nora, and R. Betti, Hydrodynamic scaling of the deceleration-phase Rayleigh-Taylor instability, *Phys. Plasmas* **22**, 072702 (2015).
- [23] Y. Srebro, Y. Elbaz, O. Sadot, L. Arazi, and D. Shvarts, A general buoyancy-drag model for the evolution of the Rayleigh-Taylor and Richtmyer-Meshkov instabilities, *Laser Part. Beams* **21**, 347 (2003).
- [24] A. L. Velikovich, J. G. Wouchuk, C. H. R. de Lira, N. Metzler, S. Zalesak, and A. J. Schmitt, Shock front distortion and Richtmyer-Meshkov-type growth caused by a small preshock nonuniformity, *Phys. Plasmas* **14**, 72706 (2007).
- [25] J.-P. Didelez and C. Deutsch, Persistence of the polarization in a fusion process, *Laser Part. Beams* **29**, 169 (2011).
- [26] C. Deutsch, H. Nersisyan, and A. Bendib, Diagnosing dense and magnetized plasmas irradiated by a petawatt laser, *Laser Part. Beams* **34**, 61 (2016).
- [27] W. Y. Zhang and R. Balescu, Statistical mechanics of a spin-polarized plasma, *J. Plasma Phys.* **40**, 199 (1988).
- [28] R. Balescu and W. Y. Zhang, Kinetic equation, spin hydrodynamics and collisional depolarization rate in a spin-polarized plasma, *J. Plasma Phys.* **40**, 215 (1988).
- [29] H. Xu, B. W. O'Shea, D. C. Collins, M. L. Norman, H. Li, and S. Li, The Biermann battery in cosmological MHD simulations of population III star formation, *Astrophys. J.* **688**, L57 (2008).
- [30] P. Wang, T. Abel, and R. Kaehler, Adaptive mesh fluid simulations on GPU, *New Astron.* **15**, 581 (2010).
- [31] R. Kulsrud, E. Valeo, and S. Cowley, Physics of spin-polarized plasmas, *Nucl. Fusion* **26**, 1443 (1986).
- [32] S. C. Cowley, R. M. Kulsrud, and E. Valeo, A kinetic equation for spin-polarized plasmas, *Phys. Fluids* **29**, 430 (1986).
- [33] M. A. Bernstein, K. F. King, and X. J. Zhou, *Handbook of MRI Pulse Sequences* (Academic Press, Burlington, MA, 2004).
- [34] C. C. Joggerst, A. Nelson, P. Woodward, C. Lovekin, T. Masser, C. L. Fryer, P. Ramaprabhu, M. Francois, and G. Rockefeller, Cross-code comparisons of mixing during the implosion of dense cylindrical and spherical shells, *J. Comput. Phys.* **275**, 154 (2014).
- [35] I. Sagert, W. P. Even, and T. T. Strother, Two-dimensional implosion simulations with a kinetic particle code, *Phys. Rev. E* **95**, 053206 (2017).
- [36] J. P. Sauppe, S. Palaniyappan, E. N. Loomis, J. L. Kline, K. A. Flippo, and B. Srinivasan, Using cylindrical implosions to investigate hydrodynamic instabilities in convergent geometry, *Matter and Radiation at Extremes* **4**, 065403 (2019).